An interface element for modelling the onset and growth of mixed-mode cracking in aluminium and fibre metal laminates

Frank Hashagen† and Rene de Borst‡

Department of Civil Engineering, Delft University of Technology, P. O. 5048, 2600 GA Delft, The Netherlands

Abstract. In the present contribution an interface crack model is introduced which is capable of modelling crack initialisation and growth in aluminium as well as in Fibre Metal Laminates. Interface elements are inserted in a finite element mesh with a yield function which bounds all states of stress in the interface. Hardening occurs after a state of stress exceeds the yield stress of the material. The hardening branch is bounded by the ultimate stress of the material. Thereafter, the state of stress is reduced to zero while the inelastic deformations grow. The energy dissipated by the inelastic deformations in this process equals the fracture energy of the material. The model is applied to calculate the onset and growth of cracking in centre cracked plates made of aluminium and GLARE®. The impact of the model parameters on the performance of the crack model is studied by comparisons of the numerical results with experimental data.

Key words: interface elements; discrete crack model; mixed-mode cracking; plasticity; fibre metal laminates.

1. Introduction

To apply new materials for modern aircraft structures it is essential to evaluate their residual strength and fracture toughness. For this reason intensive testing is undertaken before new materials enter service. A standard test for the evaluation of the K-factors and the critical energy release rate (Broek 1983), is a centre cracked plate, (ASTM 1990). While carrying out this test the crack mouth opening displacement (CMOD), the elongation and, most importantly, the crack length extension of a plate with a crack perpendicular to the loading direction are measured. On basis of these quantities the K-factors and general design rules for the application of the material are derived. However, testing is time consuming and expensive. Furthermore, experimental data should be verified against theoretical findings. Therefore, it is essential that numerical tools become available which correctly describe the onset and growth of cracking, the formation of the plastic zone around the crack tip, the elongation of the plate and the crack mouth opening displacement (CMOD). While testing a centre croched plate buckling might be caused due to imperfections in the plate, where buckling is understood as the deformation of material points around the crack perpendicular to the plane of the plate. When the displacements on one side

† Ph.D-Student
‡ Professor

of the crack have the opposite direction of those on the other side of the crack, anti-symmetric buckling occurs. This implies that a combined mode-I/mode-II failure causes the crack growth. A numerical model must take into account this effect, which requires a three-dimensional model for the formulation of the continuum as well as for the onset and growth of cracking.

To describe the crack initialisation and growth, two different classes of crack models can be distinguished, namely a discrete crack model or a smeared crack model. Applying a smeared crack model, the material behaviour is described on the integration point level of the continuum element. Various models have been derived (Feenstra 1993), (Rots 1988), (Willam, *et al.* 1987), (Cope, *et al.* 1980). The smeared crack models do not supply information about the crack width.

When a discrete crack model is applied, new degrees of freedom are introduced by inserting interface elements into a finite element mesh. These interface elements have no thickness and in the elastic regime they represent a perfect bond between two continuum element. For this reason a very high dummy stiffness is inserted in the constitutive relation between the relative displacement of the two adjacent layers of the interface element and the stress in the interface. Cracking occurs when a critical parameter, e.g., the normal stress, exceeds a certain threshold. Obviously, when interface elements are applied, cracking is located between two continuum elements, and is restricted to those locations where interface elements are inserted into the FE mesh. Therefore, crack growth is dependent on the original location and orientation of the finite elements. This draw-back is alleviated if the direction of the crack growth is known either on basis of experimental data or calculations with a smeared crack model.

Interface elements can be divided into two classes, namely nodal or point interface elements and continuous interface elements. The latter type is applied in the present model. The continuous interface elements can be applied together with shell or volume elements. Intensive research has been carried out with respect to the element formulation, mesh dependency, the impact of the integration schemes and the dummy stiffness on the performance of interface elements (Schäfer 1975, Beer 1985, Hohberg 1990, and Schellekens and de Borst 1993).

The formulation of the constitutive relation which governs the material behaviour and the description of the physically nonlinear effects has also been investigated. Depending on the failure mechanisms for which the interface elements are applied the mathematical formulation can be based on a plasticity theory (Schellekens 1992) or on a damage theory (Allix 1992).

The present research has been carried out within the framework of research on Fibre Metal Laminates for which experimental data, especially the crack orientation, are available. Combined with a need for a direct comparison of the location of the crack tip and the CMOD with numerical data makes a discrete crack model preferable compared with a smeared crack model. Therefore an interface element is described which can be applied together with solid-like shell elements (Parisch 1995), to model the onset and growth of cracking in a centre cracked plate. The solid-like shell assures a three-dimensional description of the continuum and adopts a purely displacement-based deformation field.

In the following the topology and the element formulation of the interface elements are introduced. The conclusions of previous research, especially by Hohberg (1990) and Schellekens and de Borst (1993), are taken into account to assess the performance of the present interface element with regard to the applied integration schema. Subsequently, the crack model is described. Mixed-mode cracking is expressed on the basis of a plasticity model. The onset of cracking occurs when a state of stress violates a yield function. A local return-mapping algorithm and a consistent tangent stiffness matrix are derived. The models are applied to calculate the onset and growth

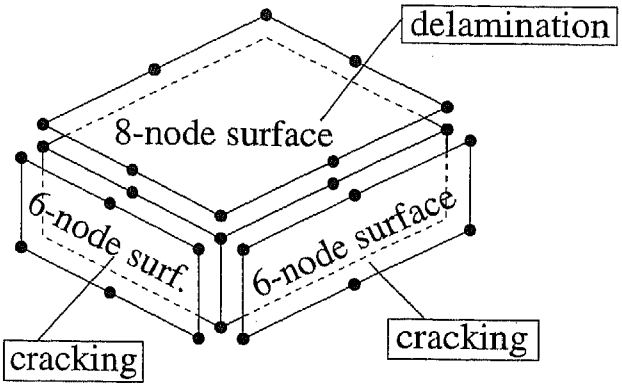

Fig. 1 Interfaces for the sixteen-noded solid-like shell element.

of cracking in a centre cracked plate made of aluminium. Next, the model is applied to investigate the cracking behaviour of a centre cracked plate made of the Fibre Metal Laminate GLARE®.

2. Element geometry and stiffness

2.1. Element geometry

If two solid-like shell elements (Parisch 1995) are connected two different kinds of interface elements can be distinguished depending on the surface of the solid-like shell element. The top and the bottom surface of a sixteen-noded solid-like shell element consist of eight nodes. However, the connection of two elements at one of the other four sides requires a twelve-noded interface element because each side is formed by six nodes, Fig. 1. Elements that are connected along these surfaces have the same material parameters, and cracking is the failure mechanism which normally occurs in this interface. In the following this twelve-noded interface element is described. For a description of an eight-noded or a sixteen-noded interface element for the connection at the top and bottom surface the reader is referred to (Schellekens and de Borst 1993).

The geometry of the twelve-noded interface element is displayed in Fig. 2. The two adjacent layers of the interface element are defined by the nodes one to six and the nodes seven to twelve, respectively. In each material point of the element a local frame of reference $l=\{n, t, s\}$ can be established. The direction n of this local frame is normal to the surface of the interface and the direction t and s are tangential to the surface in the material point. The relative displacement vector $v=(v_n, v_t, v_s)$ is defined as difference of the displacement of the two adjacent layers of the interface, with:

$$v=R\ L\ u_g. \tag{1}$$

In Eq. (1) the vector u_g contains the displacements of a point in the two planes of the interface in global coordinates $x=\{x, y, z\}$. The matrix L maps the displacements of the material points in the two planes onto the relative displacements, and the matrix R contains the transformation from the global frame of reference into the local frame of reference with:

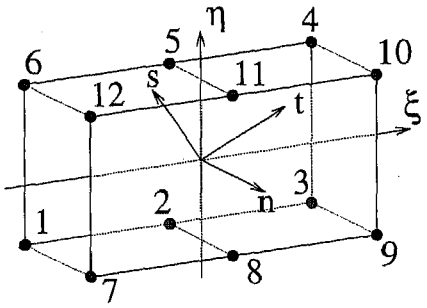

Fig. 2 Topology of the twelve-noded interface element.

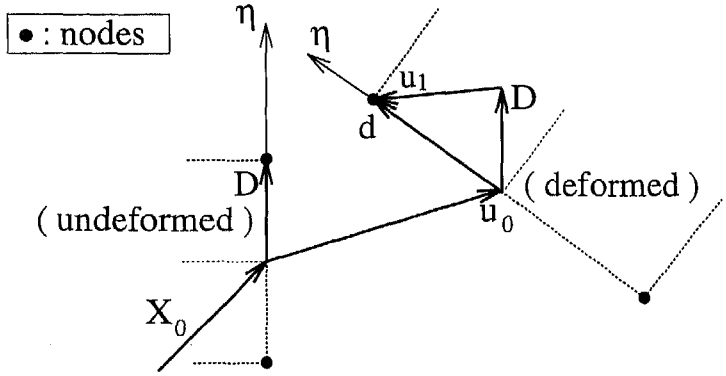

Fig. 3 Kinematics and displacement field of the twelve-noded interface element.

$$\boldsymbol{L}=\begin{bmatrix} -1 & 0 & 0 & +1 & 0 & 0 \\ 0 & -1 & 0 & 0 & +1 & 0 \\ 0 & 0 & -1 & 0 & 0 & +1 \end{bmatrix} \quad \text{and:} \quad \boldsymbol{R}=\frac{\partial \boldsymbol{l}}{\partial x}.$$

To set up the element stiffness matrix the displacement field is separated into the displacement fields of the two adjacent layers which are denoted as left and right layer. In Fig. 3 the displacement field of the right layer is shown, while the displacement field of the left layer appears in a similar manner. Any material point in the undeformed configuration can be described by a vector $\boldsymbol{X}_0$ pointing to a point on the ξ-axis of the element and the thickness director $\boldsymbol{D}$, Fig. 3. The position of a material point in the deformed configuration can additively be decomposed into the position in the undeformed configuration $(\boldsymbol{X}_0+\eta\boldsymbol{D})$ and the displacement field $\boldsymbol{u}$, with:

$$\boldsymbol{u}^r=\boldsymbol{u}_0^r+\eta\ \boldsymbol{u}_1^r. \tag{2}$$

In Eq. (2) the superscript refers to the plane, here the right plane. The displacement of a point on the ξ-axis is denoted by $\boldsymbol{u}_0^r$ and η is the coordinate in the thickness direction. The thickness director in the deformed configuration $\boldsymbol{d}^r$ can be decomposed into the thickness director in the undeformed configuration $\boldsymbol{D}^r$ and the change of the thickness director $\boldsymbol{u}_1^r$, Fig. 3. The displacement field of the left plane is set up in a similar manner which gives for the vector $\boldsymbol{u}_g$ in Eq. (1):

$$\boldsymbol{u}_g=\begin{pmatrix} \boldsymbol{u}_0^{\,l} \\ \boldsymbol{u}_0^{\,r} \end{pmatrix}+\eta\begin{pmatrix} \boldsymbol{u}_1^{\,l} \\ \boldsymbol{u}_1^{\,r} \end{pmatrix}. \tag{3}$$

If the vector of nodal displacements is introduced with the indices (x, y, z) for the global directions:

$$\hat{\boldsymbol{u}}=(u_x^{\,1},\ \ldots,\ u_x^{\,12},\ u_y^{\,1},\ \ldots,\ u_y^{\,12},\ u_z^{\,1},\ \ldots,\ u_z^{\,12}); \tag{4}$$

the vector $\boldsymbol{u}_g$ reads:

$$\boldsymbol{u}_g=\Lambda^0\hat{\boldsymbol{u}}+\eta\Lambda^1\hat{\boldsymbol{u}}. \tag{5}$$

In Eq. (5) the matrices Λ^0 and Λ^1 are composed of the quadratic interpolation functions ψ_i in the following way:

$$\Lambda^0=\begin{bmatrix} \Pi^0 & 0 & 0 & 0 & 0 & 0 \\ 0 & 0 & \Pi^0 & 0 & 0 & 0 \\ 0 & 0 & 0 & 0 & \Pi^0 & 0 \\ 0 & \Pi^0 & 0 & 0 & 0 & 0 \\ 0 & 0 & 0 & \Pi^0 & 0 & 0 \\ 0 & 0 & 0 & 0 & 0 & \Pi^0 \end{bmatrix};\quad \Lambda^1=\begin{bmatrix} \Pi^1 & 0 & 0 & 0 & 0 & 0 \\ 0 & 0 & \Pi^1 & 0 & 0 & 0 \\ 0 & 0 & 0 & 0 & \Pi^1 & 0 \\ 0 & \Pi^1 & 0 & 0 & 0 & 0 \\ 0 & 0 & 0 & \Pi^1 & 0 & 0 \\ 0 & 0 & 0 & 0 & 0 & \Pi^1 \end{bmatrix};$$

with:

$$\Pi^0=1/2(\psi_1,\ \psi_2,\ \psi_3,\ \psi_3,\ \psi_2,\ \psi_1);\ \Pi^1=1/2(-\psi_1,\ -\psi_2,\ -\psi_3,\ \psi_3,\ \psi_2,\ \psi_1).$$

After some algebra (Hashagen 1996) the matrix $\boldsymbol{B}_l$ can be derived which relates the relative displacements $\boldsymbol{v}$ in the local frame of reference l to the nodal displacements $\hat{\boldsymbol{u}}$ in the global frame of reference:

$$\boldsymbol{v}=\boldsymbol{B}_l\ \hat{\boldsymbol{u}}; \tag{6}$$

with r_{ij} the components of $\boldsymbol{R}$ and $\hat{\Pi}=\Pi^0+\eta\Pi^1$ the matrix $\boldsymbol{B}_l$ reads:

$$\boldsymbol{B}_l=\begin{bmatrix} -r_{11}\hat{\Pi} & r_{11}\hat{\Pi} & -r_{12}\hat{\Pi} & r_{12}\hat{\Pi} & -r_{13}\hat{\Pi} & r_{13}\hat{\Pi} \\ -r_{21}\hat{\Pi} & r_{21}\hat{\Pi} & -r_{22}\hat{\Pi} & r_{22}\hat{\Pi} & -r_{23}\hat{\Pi} & r_{23}\hat{\Pi} \\ -r_{31}\hat{\Pi} & r_{31}\hat{\Pi} & -r_{32}\hat{\Pi} & r_{32}\hat{\Pi} & -r_{33}\hat{\Pi} & r_{33}\hat{\Pi} \end{bmatrix}.$$

2.2. The element stiffness

In the elastic regime the constitutive relation between the tractions $\boldsymbol{t}=(t_n,\ t_t,\ t_s)$ and the relative displacements $\boldsymbol{v}$ of the two adjacent layers can be written as:

$$\boldsymbol{t}=\boldsymbol{D}\ \boldsymbol{v}\ \text{ with: }\ \boldsymbol{D}=\begin{pmatrix} d_n & 0 & 0 \\ 0 & d_t & 0 \\ 0 & 0 & d_s \end{pmatrix}. \tag{7}$$

In Eq. (7) the quantities d_i denote the individual stiffness in the directions n, t, and s. To model the perfect bond between two adjacent layers in the elastic regime the value of d_i must be relatively high compared with the Young's modulus of the material.

To derive the stiffness matrix of the element the weak form of the equilibrium is established:

$$\delta W_{ex}+\delta W_{in}=0. \tag{8}$$

The variation of the external work can be set up in a standard way using the external force vector f_{ex}:

$$\delta W_{ex}=\delta \hat{\boldsymbol{u}}^T f_{ex}; \tag{9}$$

and the variation of the internal work reads (Schellekens and de Borst 1993):

$$\delta W_{in}=\int_{S_0} \delta \boldsymbol{v}^T \boldsymbol{t}\ dS_0. \tag{10}$$

In Eq. (10). S_0 denotes the surface of the undeformed reference system. The traction vector $\boldsymbol{t}$ is a measure for the stresses which has the role similar to the 2nd Piola-Kirchhoff stress tensor for continuous media and is, as well as the relative displacement $\boldsymbol{v}$, measured with respect to the local undeformed system in each material point. In nonlinear finite element analysis the equilibrium is evaluated at time $t+\Delta t$. Decomposing the traction vector at time $t+\Delta t$ into the traction at time t_0 and a change of the tractions Δt gives together with Eq. (7):

$$\boldsymbol{t}_n=\boldsymbol{t}_0+\boldsymbol{D}\Delta \boldsymbol{v}_n. \tag{11}$$

The update of the relative displacement increment is accomplished according to:

$$\Delta \boldsymbol{v}_n=\Delta \boldsymbol{v}_{n-1}+d\boldsymbol{v}. \tag{12}$$

In Eq. (12), $d\boldsymbol{v}$ denotes the iterative change of the relative displacement at iteration n. Using Eq. (7) and Eq. (9)-Eq. (12) the virtual work equation transforms into:

$$\int_{S_0} (\delta\ d\boldsymbol{v})^T \boldsymbol{D}\ (d\boldsymbol{v})\ dS_0=(\delta d\hat{\boldsymbol{u}})^T\ f_{ex}-\int_{S_0} (\delta d\boldsymbol{v})^T \boldsymbol{t}_{n-1}\ dS_0.$$

Together with Eq. (6) the stiffness matrix for the numerically integrated interface element equals:

$$\boldsymbol{K}=\int_\eta \int_\xi \boldsymbol{B}_l^T \boldsymbol{D} \boldsymbol{B}_l\ \det\ \boldsymbol{J}_0\ d\xi d\eta; \tag{13}$$

and the internal force reads:

$$f_{in}=\int_\eta \int_\xi \boldsymbol{B}_l^T \boldsymbol{t}_{n-1}\ \det\ \boldsymbol{J}_0\ d\xi d\eta. \tag{14}$$

2.3. Performance tests

Before the constitutive relation for modelling crack initialisation and growth can be derived for the interface element the performance of the element regarding the dummy stiffness and the applied integration schema must be verified (Schellekens and de Borst 1993). Due to the presence of the high dummy stiffness spurious oscillations of the stress field can occur, (Hohberg 1990). Therefore, a 3D notched concrete beam (Rots and Schellekens 1990) is modelled with solid-like shell elements and the corresponding interface elements. The structure is analysed using a Gauss, a Newton-Cotes, a Lobatto or a lumped integration for different values of the dummy stiffness. The geometry of the structure is displayed in Fig. 4. A refinement of the mesh is applied at the side where the notch is located. The interface elements are located at the front of the notch in order to model the potential development of a discrete crack. Since the

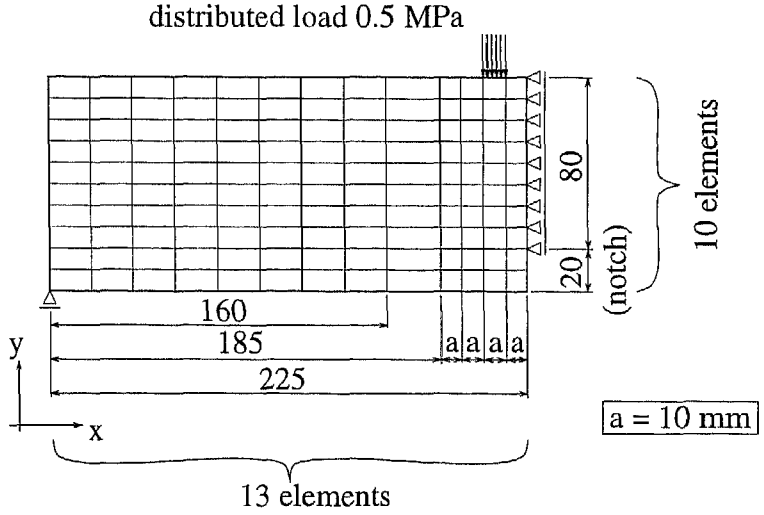

Fig. 4 Geometry of the 3D notched concrete beam (t=100.0 mm).

application of interface elements should not lead to additional high deformations in the elastic regime a very high dummy stiffness d_i must be supplied for the calculations. To assess the impact of the dummy stiffness; $d_i=10^{+3}$ N/mm^3 and $d_i=10^{+5}$ N/mm^3 have been chosen for all three directions. The Young's modulus of the continuum equals $E=20$ GPA while a Poisson ratio $\nu=0.2$ is adopted. A surface load is applied at the second row of elements, Fig. 4, with a total load of $F_T=1.0$ kN. The structure is simply supported at the left bottom side and symmetry is assumed perpendicular to the plane of the notch.

The results of the calculations are shown in Fig. 5-Fig. 7. Using a dummy stiffness of $d_i=10^{+3}$ N/mm^3 all integration schemes produce satisfactory results. However, for a stiffness of $d_i=10^{+5}$ N/mm^3 spurious oscillations occur when a Gauss, a Newton-Cotes, or a Lobatto integration is applied. Schellekens has reported spurious oscillations for a sixteen-noded interface element when a Gauss or a lumped integration are applied. Schellekens attributes the poor behaviour

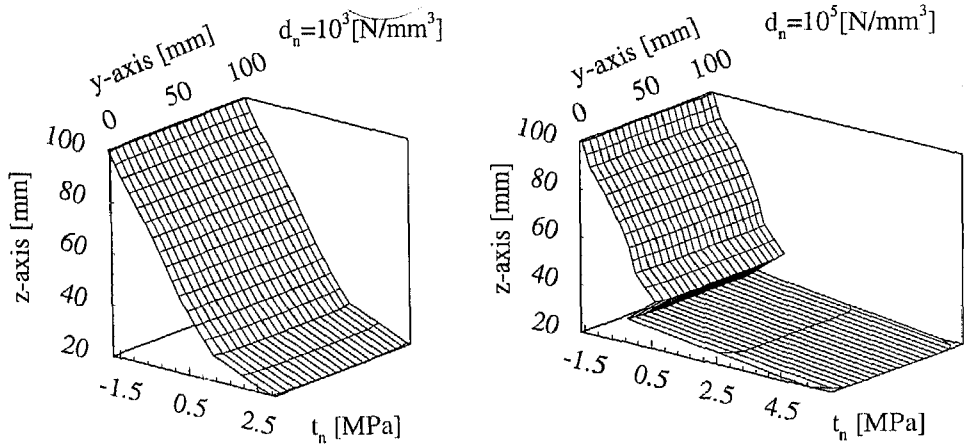

Fig. 5 Traction profile for the twelve-noded interface element calculated with 3×3 Lobatto/Newton-Cotes integration; left: $d_n=10^{+3}$[N/mm^3]; right: $d_n=10^{+5}$[N/mm^3].

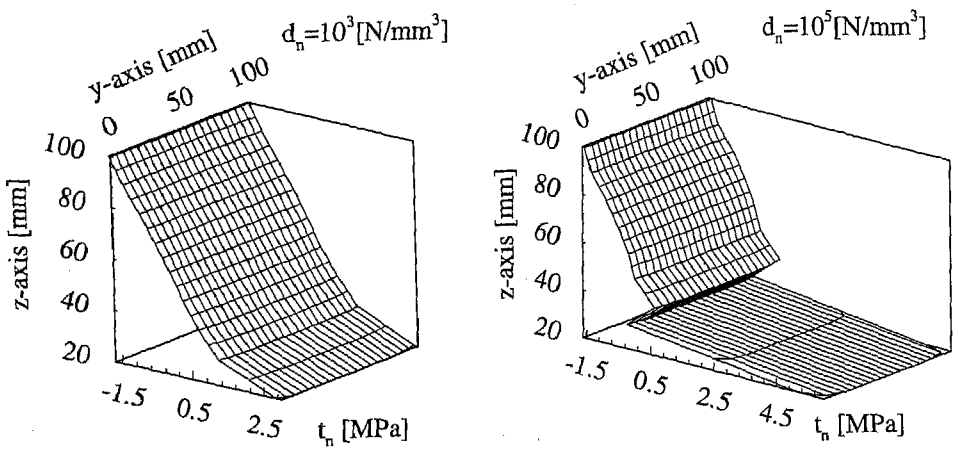

Fig. 6 Traction profile for the twelve-noded interface element calculated with 3×3 Gauss integration; left: $d_n=10^{+3}$[N/mm^3]; right: $d_n=10^{+5}$[N/mm^3].

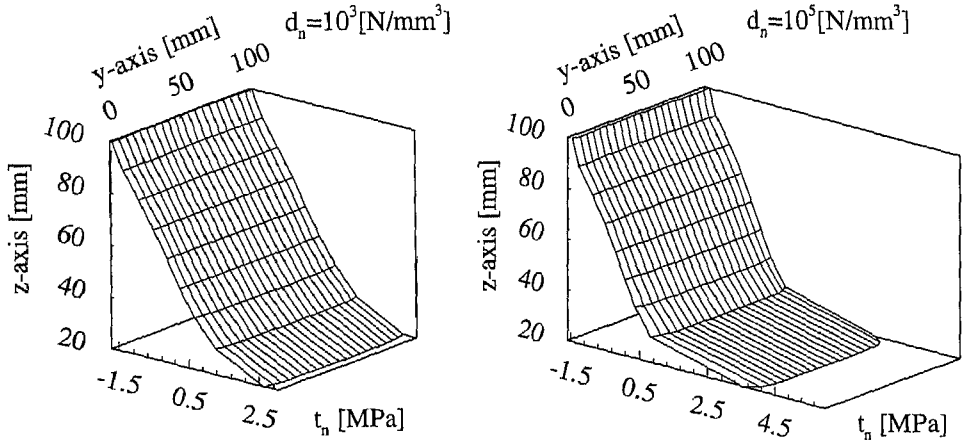

Fig. 7 Traction profile for the twelve-noded interface element calculated with lumped integration; left: $d_n=10^{+3}$[N/mm^3]; right: $d_n=10^{+5}$[N/mm^3].

of the lumped integration for a sixteen-noded interface element to the negative surface contributions. In contrast to a sixteen-noded interface element, the surface contributions of the present twelve-noded interface element remain positive. Therefore, no negative diagonal terms occur on the diagonal of the stiffness matrix and a well-conditioned system of equations arises that can be solved by applying a LDU-decomposition. The spurious oscillation that occur when a Gauss, a Newton-Cotes or a Lobatto integration are applied are caused by the choice of a linear shape function in η-direction, Fig. 2. The stiffness matrix can be decomposed into a matrix which contains the contributions of integration points that coincide with the nodes of the element and the contribution of integration points which are located between two nodes. The latter parts of the stiffness matrix cause coupling between the nodes. Due to the linear displacement field in η-direction the displacements are not approximated correctly when the elements exhibit a highly nonlinear displacement field in the η-direction. Therefore, a lumped integration is recommended for the twelve-noded interface element.

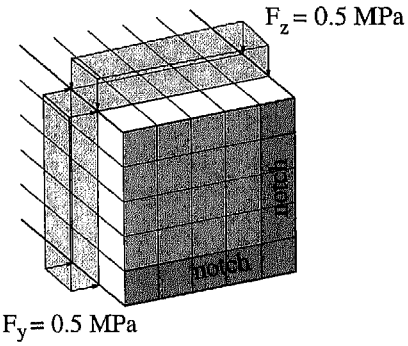

Fig. 8 Force and notch localisation of the modified notched concrete beam.

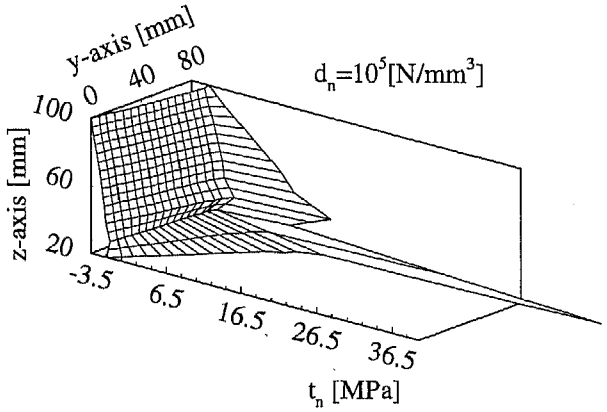

Fig. 9 Traction profile of the doubly notched concrete beam applying 3×3-Newton-Cotes integration and $d_i=10^{+5}$[N/mm^3].

For a further clarification of the impact of the integration method on the traction profile, the notched concrete beam is modified. To trigger a second traction gradient another notch is attached perpendicular to the first notch, combined with a distributed force in the y-direction, Fig. 8. The results with a dummy stiffness of $d_i=10^{+5}$ N/mm^3 and either 3×3 Newton-Cotes or lumped integration are displayed in Fig. 9 and Fig. 10. It can be seen that the three point integration in the ξ-direction which corresponds to the global y-direction does not yield spurious oscillations. In this direction the nonlinear displacement field can be approximated correctly.

3. The interface crack model

3.1. Return-mapping and tangent stiffness

In a general situation all three stress components in the plane of cracking are affected by the initialisation of a crack. For a fully opened crack even under single-mode loading this means that no stress can be transferred in any of the three directions in the plane of cracking.

A yield function is now introduced which bounds all states of stress. In the limiting case the yield function shrinks to a point in the origin of the stress space while the inelastic deforma-

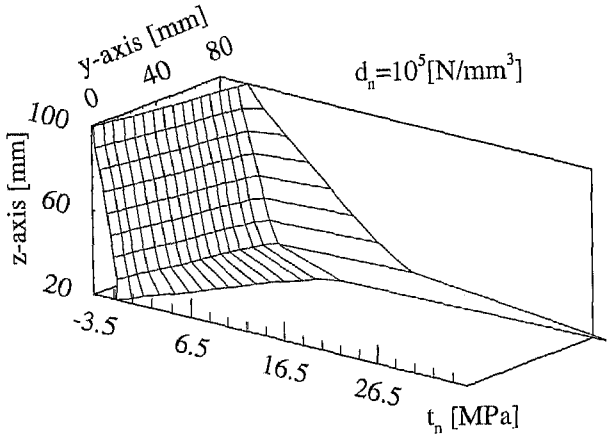

Fig. 10 Traction profile of the doubly notched concrete beam applying lumped integration and $d_i=10^{+5}$ [N/mm^3].

tions grow. The yield function Φ reads:

$$\Phi(\boldsymbol{t},\ \kappa)=\sqrt{3/2\ \boldsymbol{t}^T\ \boldsymbol{P}\ \boldsymbol{t}}-\bar{t}(\kappa)\ \leq\ 0. \tag{15}$$

In Eq. (15), the quantity $\bar{t}$ denotes the equivalent stress. It is a function of the hardening parameter κ and discussed in the remainder. The vector $\boldsymbol{t}$ contains the tractions, Eq. (7). The matrix $\boldsymbol{P}$ is set up with reference to von Mises plasticity:

$$\boldsymbol{P}=\begin{bmatrix} 2/3 & 0 & 0 \\ 0 & 2 & 0 \\ 0 & 0 & 2 \end{bmatrix} \tag{16}$$

The shape of the yield function is displayed in Fig. 11. For the application of this plasticity-based crack model the consistent tangent stiffness matrix and the local return-mapping are derived. For this purpose, the field of relative displacements is decomposed into an elastic and a plastic part, $\boldsymbol{v}^{el}$ and $\boldsymbol{v}^{pl}$, respectively. In an incremental formulation this reads:

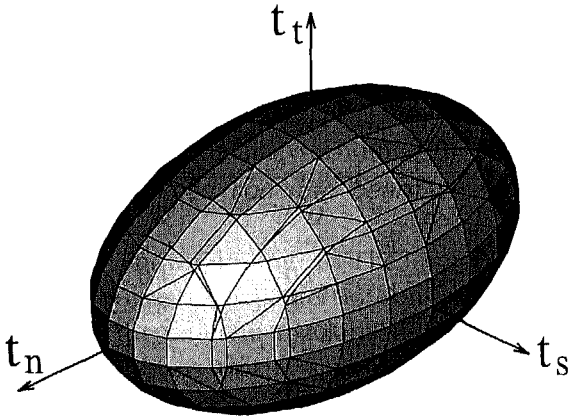

Fig. 11 Yield surface of the von Mises-type yield criterion.

$$\Delta \boldsymbol{v} = \Delta \boldsymbol{v}^{el} + \Delta \boldsymbol{v}^{pl}. \tag{17}$$

Under the assumption of an associative flow rule the plastic deformations can be written in an incremental manner as:

$$\Delta \boldsymbol{v}^{pl} = \Delta\lambda \left(\frac{\partial \Phi}{\partial \boldsymbol{t}} \right). \tag{18}$$

Hereby, $\Delta\lambda$ represents the finite amount of inelasticity and the gradient $(\partial\Phi/\partial \boldsymbol{t})$ sets the direction of the plastic deformations. The increment of the elastic relative displacements $\Delta \boldsymbol{v}^{el}$ is related to the traction increment $\Delta \boldsymbol{t}_n$ at the end of the loading step via the linear elastic stiffness matrix $\boldsymbol{D}$:

$$\Delta \boldsymbol{v}^{el} = \boldsymbol{D}^{-1} \Delta \boldsymbol{t}. \tag{19}$$

Upon substitution of Eq. (17) and Eq. (18) into Eq. (19) we obtain:

$$\Delta \boldsymbol{t}_n = \boldsymbol{D} \left[\Delta \boldsymbol{v}_n - \Delta\lambda_n \left(\frac{\partial \Phi}{\partial \boldsymbol{t}} \right) \right]. \tag{20}$$

The tractions at the end of a loading step $\boldsymbol{t}_n$ are decomposed into:

$$\boldsymbol{t}_n = \boldsymbol{t}_0 + \Delta \boldsymbol{t}_n; \tag{21}$$

where $\boldsymbol{t}_0$ contains the tractions at the beginning of the loading step. Substituting Eq. (20) into Eq. (21) finally leads to:

$$\boldsymbol{t}_n = \boldsymbol{t}_{trial} - \Delta\lambda_n \boldsymbol{D} \left(\frac{\partial \Phi}{\partial \boldsymbol{t}} \right); \text{ with } \boldsymbol{t}_{trial} = \boldsymbol{t}_0 + \boldsymbol{D} \Delta \boldsymbol{v}_n. \tag{22}$$

If the trial traction $\boldsymbol{t}_{trial}$ violates the yield function, Eq. (15), then the corresponding tractions and the inelastic deformations are calculated according to:

$$\boldsymbol{t}_n - \boldsymbol{t}_{trial} + \Delta\lambda_n \boldsymbol{D} \left(\frac{\partial \Phi}{\partial \boldsymbol{t}} \right) = 0; \tag{23}$$

and:

$$\Phi(\boldsymbol{t}_n, \kappa_n) = 0. \tag{24}$$

Eq. (23) and Eq. (24) represent a system of four equations with the five unknowns: $\boldsymbol{t}$, κ, $\Delta\lambda$. For the final solution of Eq. (23) and Eq. (24) a hardening hypothesis must be introduced which describes the relation between $\Delta\lambda_n$ and $\Delta\kappa_n$.

In mixed-mode fracture, which occurs for instance when anti-symmetric buckling appears in a centre cracked plate, it is appealing to take the dissipated inelastic energy as hardening parameter. It can be directly compared with the fracture energy G_f which serves as a fundamental material parameter for the model. The hardening parameter is defined:

$$\kappa = \int \dot{\kappa} \, dt; \tag{25}$$

and the rate of the hardening parameter $\dot{\kappa}$ is set up according to the following hardening hypothesis:

$$\dot{\kappa} = \boldsymbol{t}^T \dot{\boldsymbol{v}}^{pl}; \tag{26}$$

which, using Eq. (18), reads in an incremental format:

$$\Delta\kappa=\Delta\lambda\ t^T\left(\frac{\partial\Phi}{\partial t}\right). \tag{27}$$

To arrive at a stable local return-mapping algorithm, the change of the hardening parameter $\Delta\kappa$ is considered as independent variable (Hofstetter and Mang 1995), instead of $\Delta\lambda$:

$$\Delta\lambda=\frac{\Delta\kappa}{\bar{t}}; \tag{28}$$

where Eq. (15) has been used. Upon substitution of this expression for $\Delta\lambda$ in Eq. (23) we obtain:

$$t_n=\boldsymbol{B}^{-1}t_{trial}. \tag{29}$$

With $\boldsymbol{I}$ the unit matrix, $\boldsymbol{B}$ can be written as:

$$\boldsymbol{B}=\left[\boldsymbol{I}+\frac{3}{2}\frac{\Delta\kappa}{\bar{t}^2}\boldsymbol{DP}\right]_{[3\times3]}. \tag{30}$$

Employing Eq. (29) in Eq. (15) the yield function is rewritten as a function of $\Delta\kappa$:

$$\sqrt{3/2\,t_{trial}^T\boldsymbol{B}^{-T}\boldsymbol{P}\boldsymbol{B}^{-1}t_{trial}}-\bar{t}(\kappa)=0. \tag{31}$$

Starting from an initial estimate $\Delta\kappa_n^0=0$ Eq. (31) can be solved using a Newton-Raphson schema:

$$\Delta\kappa_n^k=\Delta\kappa_n^{k-1}-\Phi/(d\Phi/d\Delta\kappa)\ |_n^{k-1}.$$

The gradient $(d\Phi/d\Delta\kappa)$ is obtained by differentiating Eq. (31). Taking into account that the matrices $\boldsymbol{D}$, $\boldsymbol{B}$ and $\boldsymbol{P}$ are diagonal matrices for the interface element $(d\Phi/d\Delta\kappa)$ reads:

$$\frac{d\Phi}{d\Delta\kappa}=-\frac{9}{4}\frac{1}{\bar{t}}\frac{1}{(\Phi+\bar{t})}\left(\frac{1}{\bar{t}}-2\frac{\Delta\kappa}{\bar{t}^2}\frac{\partial\bar{t}}{\partial\kappa}\right)t_{trial}^T\left[\boldsymbol{P}^2\boldsymbol{D}\boldsymbol{B}^{-3}\right]t_{trial}-\frac{\partial\bar{t}}{\partial\kappa}. \tag{32}$$

The rate of convergence on local level depends on the function which describes the equivalent stress $\bar{t}(\kappa)$. For large load increments and a subsequent large trial stress increment combined with a small equivalent stress $\bar{t}$ quadratic convergence cannot always be guaranteed. In Fig. 12 the yield function $\Phi(\Delta\kappa)$ is displayed for a typical situation. In the limiting case when the trial stress tends against infinity and the equivalent stress tends against zero the rate of convergence can be approximated by: $\Phi^k\approx1/2\Phi^{k-1}$. Based on this phenomenon a pre-iteration is applied with: $\Delta\kappa^{kp}=\Delta\kappa_0 2^{kp}$, $\Phi(\Delta\kappa)>0$ and max kp, after which nearly quadratic convergence is obtained.

In a full Newton-Raphson procedure the tangential stiffness matrix must be set up for every iteration on global level. Starting with the differentiation of Eq. (23), whereby t_{trial} is not constant but a function of v, gives:

$$dt_n=\boldsymbol{H}_{en}^{-1}\left[dv_n-\left[t^T\left(\frac{\partial\Phi}{\partial t}\right)\right]^{-1}\left(\frac{\partial\Phi}{\partial t}\right)d\Delta\kappa_n\right]. \tag{33}$$

In Eq. (33), the matrix $\boldsymbol{H}_{en}$ equals:

$$\boldsymbol{H}_{en}=\left[\boldsymbol{D}^{-1}+\Delta\kappa\left[\left[t^T\left(\frac{\partial\Phi}{\partial t}\right)\right]^{-1}\frac{\partial^2\Phi}{\partial t^2}-\left[t^T\left(\frac{\partial\Phi}{\partial t}\right)\right]^{-2}\left(\frac{\partial\Phi}{\partial t}\right)\left(t^T\frac{\partial^2\Phi}{\partial t^2}+\left(\frac{\partial\Phi}{\partial t}\right)^T\right)\right]\right]. \tag{34}$$

Invoking Prager's consistency relation, $\dot{\Phi}(t,\ \kappa)=0$, $d\Delta\kappa_n$ can be rewritten as:

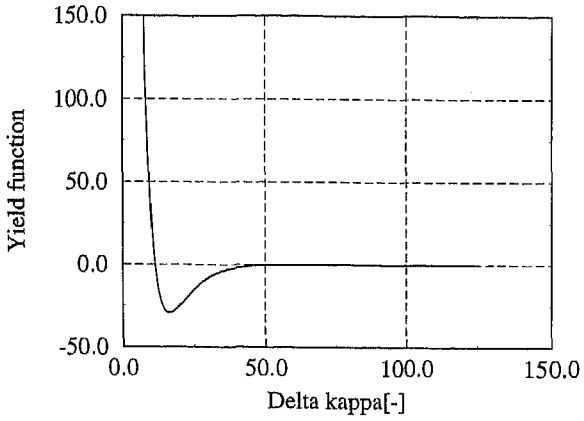

Fig. 12 Function $\Phi(\Delta\kappa)$ in a typical situation for the local return-mapping procedure.

$$d\Delta\kappa_n = \frac{\left(\frac{\partial\Phi}{\partial t}\right)^T \boldsymbol{H}_{en}^{-1} d\boldsymbol{v}_n}{\left[\boldsymbol{t}^T\left(\frac{\partial\Phi}{\partial t}\right)\right]^{-1}\left(\frac{\partial\Phi}{\partial t}\right)^T \boldsymbol{H}_{en}^{-1}\left(\frac{\partial\Phi}{\partial t}\right) - \frac{\partial\Phi}{\partial\kappa}} \tag{35}$$

Upon substitution of $d\Delta\kappa_n$ in Eq. (33) by Eq. (35) the tangential stiffness relation finally becomes:

$$d\boldsymbol{t}_n = \left[\boldsymbol{H}_{en}^{-1} - \frac{\boldsymbol{H}_{en}^{-1}\left(\frac{\partial\Phi}{\partial t}\right)\left(\frac{\partial\Phi}{\partial t}\right)^T \boldsymbol{H}_{en}^{-1}}{\left(\frac{\partial\Phi}{\partial t}\right)^T \boldsymbol{H}_{en}^{-1}\left(\frac{\partial\Phi}{\partial t}\right) - \frac{\partial\Phi}{\partial\kappa}\,\boldsymbol{t}^T\left(\frac{\partial\Phi}{\partial t}\right)}\right] d\boldsymbol{v}_n. \tag{36}$$

Note, that due to the product:

$$\left(\frac{\partial\Phi}{\partial t}\right)\left(\boldsymbol{t}^T\frac{\partial^2\Phi}{\partial t^2} + \left(\frac{\partial\Phi}{\partial t}\right)^T\right);$$

which appears in Eq. (34) for $\boldsymbol{H}_{en}$, the stiffness operator can become non-symmetric.

3.2. The hardening/softening function

The function $t(\kappa)$ is a phenomenological representation of the fracture process and not a description of the atomic separation (Tvergaard and Hutchinson 1993). In contrast to the traction-separation law proposed by Tvergaard and Hutchinson (1993) the interface element has to represent a perfect bond between the two adjacent layers in the elastic regime. Thus, the fracture process is initialised when the initial yield stress σ_y is reached. Then, the stress increases from the yield stress σ_y up to the ultimate stress σ_u of the material, Fig. 13. When the ultimate stress is reached the plastic work per unit surface area equals the fracture energy G_f of the material. At this point cracking is initiated and the dissipated energy exceeds the fracture energy. The stress is reduced to zero while the inelastic relative displacements grow. To obtain a smooth transition from the hardening to the softening branch, the hardening regime is described by a quadratic

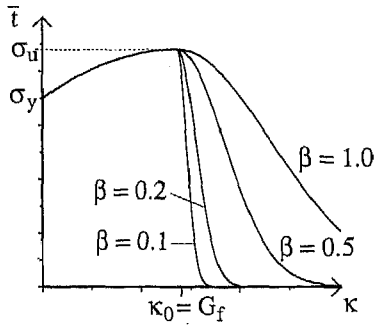

Fig. 13 Hardening and softening function for the interface crack model.

function:

$$\bar{t} = -\frac{\sigma_u - \sigma_y}{G_f^2}\kappa^2 + 2\frac{\sigma_u - \sigma_y}{G_f}\kappa + \sigma_y. \tag{37}$$

and the softening regime is described by an exponential function, (Keuser, *et al.* 1983):

$$\bar{t} = \sigma_{res} + (\sigma_u - \sigma_{res})\, e^k; \text{ with: } k = -\left(\frac{\kappa - G_f}{\beta\, G_f}\right)^2. \tag{38}$$

The parameter β determines the rate of softening. For a sharp decrease a parameter $\beta = 0.15$ is chosen. The hardening and softening branch are exposed schematically in Fig. 13. The residual stress σ_{res} is a small value ($\sigma_{res} = 10^{-2}$ MPa) in order to achieve numerical stability for the return-mapping algorithm.

4. Numerical investigations

4.1. Centre cracked plate with pure mode-I cracking

A standard test to investigate the residual strength and the crack growth of materials is a centre cracked plate, (ASTM 1990). In the following the plate is taken to assess the performance of the present crack model. In Fig. 14 the geometrical properties of the plate are exposed. The numerical results obtained with the interface model are compared with results obtained experimentally for this problem at the Faculty of Aerospace Engineering of Delft University of Technology, (de Vries 1994).

By virtue of symmetry of the plate one quarter is modelled with sixteen-noded solid-like shell elements. At the symmetry line from the tip of the crack onwards, interface elements are located. The displacements in the y-direction of one plane of the interface elements are restrained. In the x-direction the displacements of both interface planes are the same. The plate is loaded with a distributed load as depicted in Fig. 14. The material data for the aluminium plate and the interface are collected in Tables 1 and 2, respectively.

It is known (Bazant 1976) that softening problems tend to suffer from mesh dependence. To assess this effect calculations have been carried out with three meshes with 1227, 798 and 512 elements, respectively and a mesh refinement at the crack tip (Hashagen 1996). In a first

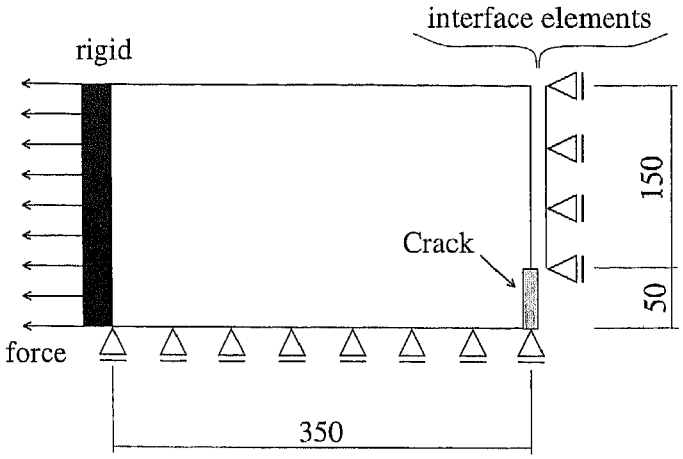

Fig. 14 Geomerical properties (in [mm]) and boundary conditions of the centre cracked plate (t=1.04 mm).

Table 1 Material data for aluminium alclad 2024-T3L

E [GPa]	ν	σ_{yield} [MPa]	$\sigma_{ultimate}$ [MPa]	$\varepsilon_{ultimate}$
66.0	0.33	350.0	440.0	0.15

Table 2 Material data for the interface elements representing cracking in aluminium

d[N/mm^3]	σ_{yield} [MPa]	$\sigma_{ultimate}$ [MPa]	G_f [N/mm]	β
$1 \cdot 10^{+5}$	350.0	440.0	95.6	0.15

series of calculations plasticity in the aluminium has not been taken into account. The elongation, the crack mouth opening displacement and the crack length extension for this case are displayed in Fig. 15-Fig. 17. It can be observed that a significant difference exists between experimental and numerical results. The reason for this effect is caused by the plastic effects in the continuum. Furthermore, the results become worse without mesh refinement at the crack tip.

In a second series of calculations von Mises plasticity is included for the continuum, Table 1. The results of these calculations are also displayed in Fig. 15-Fig. 17. Now, a good agreement between numerical and experimental results is obtained. However, a snap-back is observed for the elongation which is not found in the experimental results. The reason for this effect lies in the choice of the softening parameter β. Here, a sharp drop is assumed. According to Tvergaard and Hutchinson (1993) a part of the fracture energy is dissipated on the softening branch. This gives a smoother drop from the ultimate stress to zero. Therefore, a higher value for β gives better results and circumvents severe mesh dependence, (Bazant 1976). The following calculations have been carried out with β=0.3.

The fracture energy G_f which serves as the fundamental material parameter can be calculated from experimental data given by de Vries (1994). Two different methods can be applied for the calculation of G_f. If the method according to Irwin (1958) is applied we obtain G_f=95.6

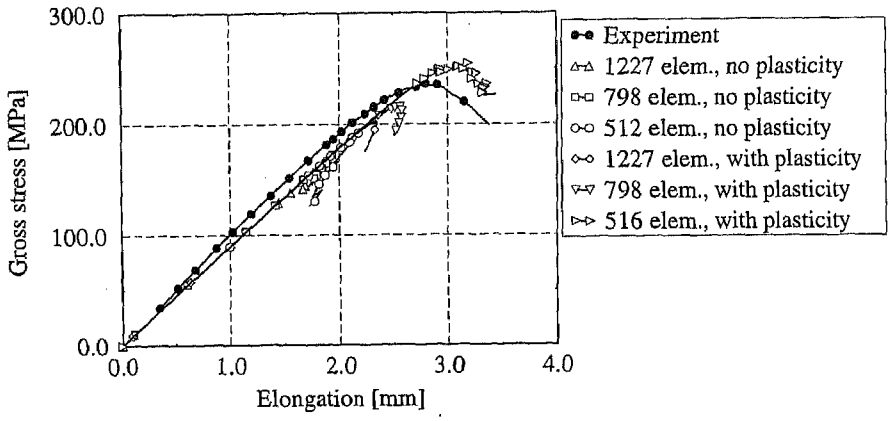

Fig. 15 Elongation of the centre cracked plate for different meshes and the interface crack model with G_f=95.6 N/mm.

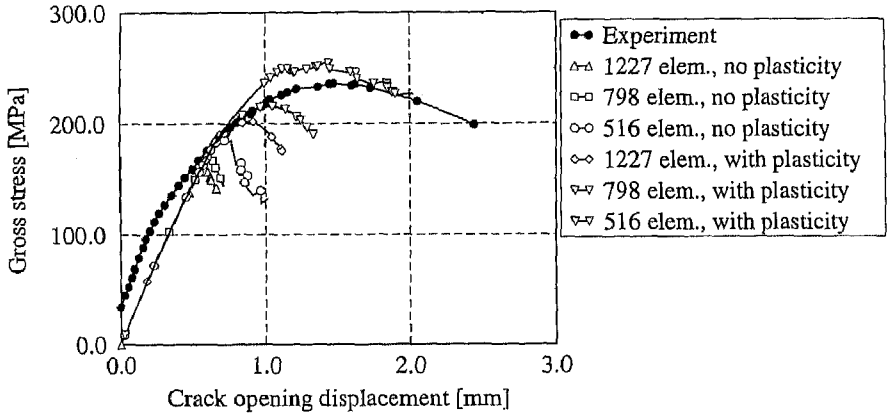

Fig. 16 Crack mouth opening displacement of the centre cracked plate for different meshes and the interface crack model with G_f=95.6 N/mm.

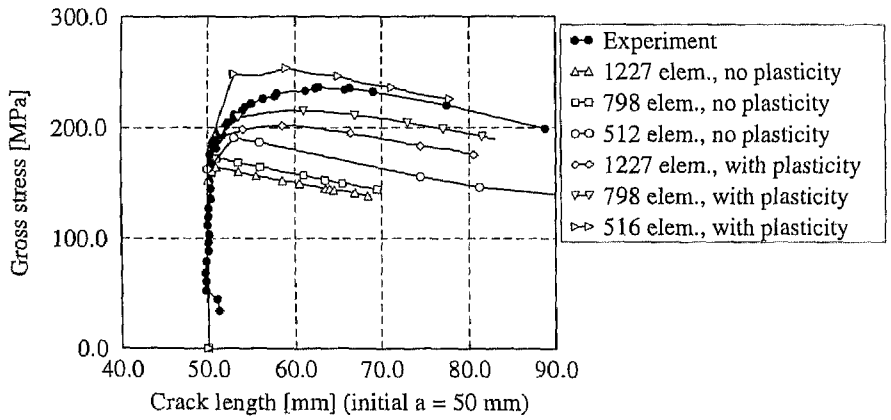

Fig. 17 Crack length of the centre cracked plate for different meshes and the interface crack model with G_f=95.6 N/mm.

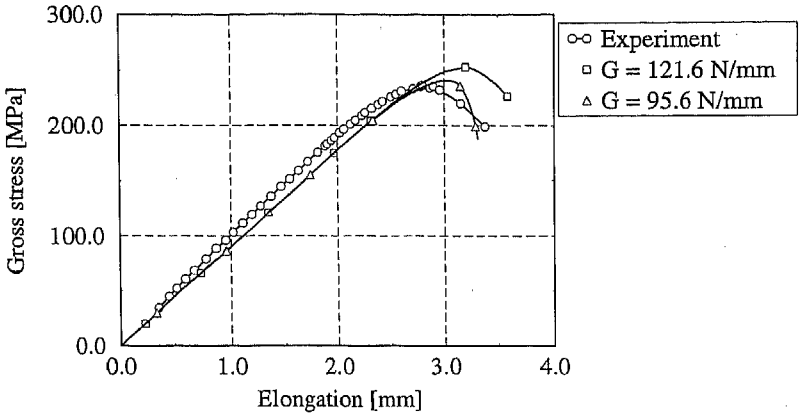

Fig. 18 Elongation of the centre cracked plate modelled with 798 elements by applying solid-like shell elements with plasticity and the interface element with $\beta=0.3$.

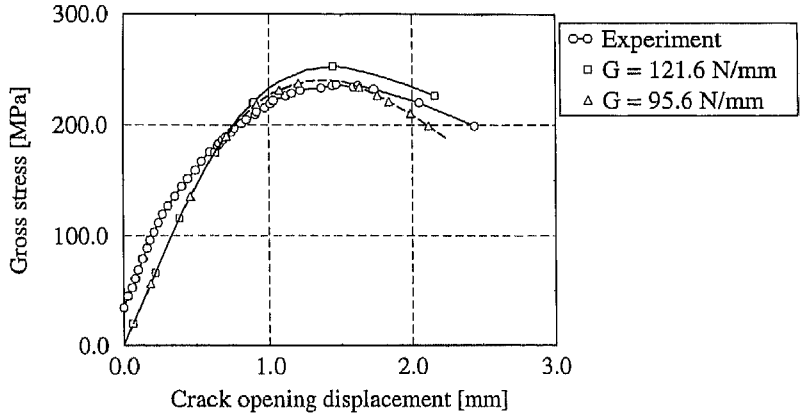

Fig. 19 Crack mouth opening displacement of the centre cracked plate modelled with 798 elements by applying solid-like shell elements with plasticity and the interface element with $\beta=0.3$.

N/mm. However, if the method according to Eftis and Liebowitz (1972) is used $G_f=121.6$ N/mm results. To investigate the impact of the fracture energy on the performance of the model calculations have been carried out with both values of G_f.

In Fig. 18-Fig. 20 the results for a variation of the fracture energy are displayed. Obviously, a variation does not lead to a significant difference between experimental and numerical results. However, with an increasing fracture energy the load bearing capacity increases and the crack grows at a slower rate.

4.2. Centre cracked plate made of GLARE®

Finally, the crack model is applied for modelling crack propagation of a centre cracked plate made of the Fibre Metal Laminate GLARE®. This material consists of thin aluminium layers that are connected by prepreg layers. Here, a lay-up is taken with *R*-Glass fibres in the prepreg layers that are oriented in loading direction. From experiments the homogenised material parameters are obtained which are collected in Table 3 and Table 4 for the continuum and the interface,

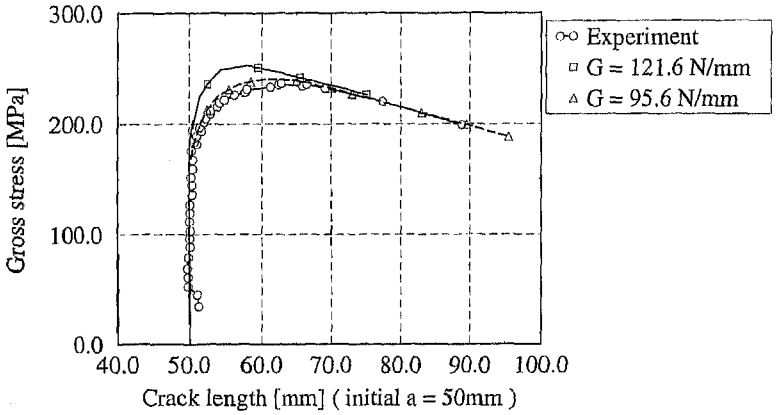

Fig. 20 Crack length of the centre cracked plate modelled with 798 elements by applying solid-like shell elements with plasticity and the interface element with $\beta=0.3$.

Table 3 Material data for GLARE® assuming a plane stress situation

E_{11}	65 GPa	E_{22}	50 GPa	G_{12}	17 GPa	ν_{12}	0.33
σ_y	360.0 MPa	σ_u	1074 MPa	κ_u	0.105	-	-

Table 4 Material data for the interface elements representing cracking in GLARE®

d [N/mm^3]	σ_{yield} [MPa]	$\sigma_{ultimate}$ [MPa]	G_f [N/mm]	β
$1\cdot10^{+8}$	360.0	1074.0	371.53	0.3

respectively. The calculations are carried out under the assumption of a plane stress situation. The geometry of the plate remains the same but with a thichness $t=1.4$ mm and is exposed in Fig. 14. Again, symmetry is assumed. Due to fibre bridging at the crack tip a smoother softening has been assumed. Therefore, the calculations have been carried out with $\beta=0.2$ and $\beta=0.5$.

In Fig. 21-Fig. 23 the results of the calculations are shown. It can be observed in Fig. 23 that the crack growth for the composite agrees well with the experimental results. However, differences occur when the elongation and the crack mouth opening displacement are considered. The reason is the assumption of isotropic von Mises plasticity for an orthotropic material. The numerical results show a better agreement with the experimental data, Fig. 21-Fig. 23, when the calculations are carried out with an orthotropic plasticity model (Hashagen 1997).

5. Conclusions

In the present paper a discrete crack model has been introduced. On the basis of interface elements which are inserted into the finite element mesh cracking is modelled by a yield function which bounds all states of stress. In the limiting case of a fully opened crack the stress reduces

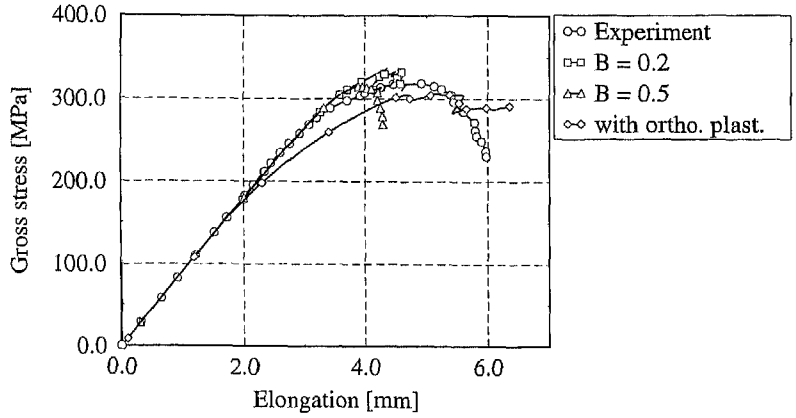

Fig. 21 Elongation of the centre cracked plate made of GLARE® modelled with 798 plane stress elements.

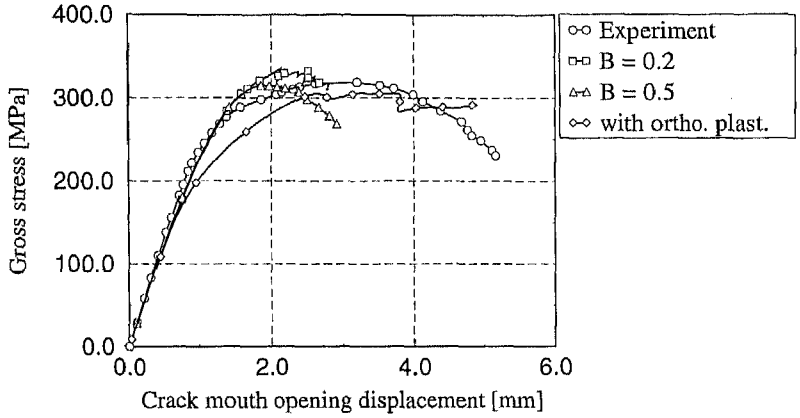

Fig. 22 Crack mouth opening displacement of the centre cracked plate made of GLARE® modelled with 798 plane stress elements.

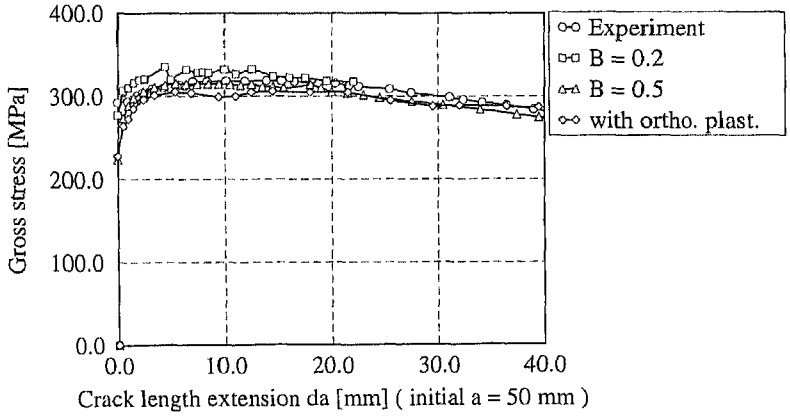

Fig. 23 Crack length extension of the centre cracked plate made of GLARE® modelled with 798 plane stress elements.

to zero while the inelastic deformations grow unboundedly.

The model has been applied to calculate crack propagation in a centre cracked plate made of aluminium or GLARE®. The results obtained numerically match the data obtained experimentally. It has been demonstrated that the proper choice of the softening parameter β circumvents mesh dependence. Also, the major impact of the development of the plastic zone around the crack tip on the results has been demonstrated.

References

Allix, O. and Ladeveze, P. (1992), "Modelling and computation of delamination for composite laminates", *Arch, Mech.*, **44**, 5-13.

ASTM E 561-86 (1990), "Standard practise for R-curve determination", *Annual book of ASTM Standards.*

Bazant, Z.P. (1976), "Instability, ductility and size effect in strain-softening concrete", *ASCE J. Eng. Mech.*, **102(2)**, 331-344.

Beer, G. (1985), "An isoparametric joint/interface element for finite element analysis", *Int. J. Numer. Meth. Eng.*, **21**, 585-600.

Broek, D. (1983), *Elementary Engineering Fracture Mechanics*, Nijhoff Publishers, Dordrecht.

Cope, R.J., Rao, P.V., Clark, L.A. and Norris, P. (1980), "Modelling of reinforced concrete behaviour for finite element analysis of bridge slabs", *Numer. Meth. Nonl. Probl.*, Eds.: Taylor C. et al., Pineridge Press, Swansea, 457-470.

Eftis, J. and Liebowitz, H. (1972), "On the modified Westergaard equation for certain plane crack problems", *Int. J. Fracture*, **8**, 383-392.

Feenstra, P.H. (1993), "Computational aspects of biaxial stress in plain reinforced concrete", *Dissertation*, Delft University of Technology, Delft.

Hashagen, F. (1996), "An interface element for crack modelling in aluminium", *TU Delft report nr.: 03-21-0-31-10*, Delft University of Technology, Delft.

Hashagen, F. and Borst, R. de (1997), "A model for anisotropic hardening combined with Hoffman plasticity", *Proceedings of COMPLAS 1997*, Barcelona, March.

Hofstetter, G. and Mang, H.A. (1995), *Computational Mechanics of Reinforced Concrete Structures*, Vieweg, Braunschweig.

Hohberg, J.-M. (1990), "A note on spurious oscillations in FEM joint elements", *Earthq. Eng. Struc. Dyn.*, **19**, 773-779.

Irwin, G.R. (1958), *Handbuch der Physik*, Ed. Flügge, Springer, Berlin.

Keuser, M., Mehlhorn, G. and Cornelius, V. (1983), "Bond between prestressed steel and concrete-computer analysis using ADINA", *Comp. Struct.*, **17**, 669-676.

Parisch, H. (1995), "A continuum-based shell theory for nonlinear applications", *Int. J. Numer. Meth. Eng.*, **38**, 1855-1883.

Rots, J.G. (1988), "Computational modelling of concrete fracture", *Dissertation*, Delft University of Technology, Delft.

Rots, J.G. and Schellekens, J.C.J. (1990), "Interface elements in concrete mechanics", *Computer Aided Analysis and Design of Concrete Structures*, Eds.: Bićanić N., Mang H., Pineridge Press, Swansea, 909-918.

Schäfer, H. (1975), "A contribution to the solution of contact problems with the aid of bond elements", *Comp. Meth. Appl. Mech. Eng.*, **6**, 335-354.

Schellekens, J.C.J. (1992), "Computational strategies for composite structures", *Dissertation*, Delft University of Technology, Delft.

Schellekens, J.C.J. and Borst, R. de (1993), "On the integration of interface elements", *Int. J. Num. Meth. Eng.*, **36**, 43-66.

Tvergaard, V. and Hutchinson, J.W. (1993), "The influence of plasticity on mixed-mode interface toughness", *J. Mech. Phys. Solids*, **41(6)**, 1119-1135.

Vries, T. de (1994), "Various parameters concerning the residual strength of aircraft materials, Part II, test data and charts", *Graduation Thesis,* Delft University of Technology, Delft.

Willam, K., Pramono, E. and Sture, S. (1987), "Fundamental issues of smeared crack models", *Proc. SEM-RILEM Int. Conf. on Fracture of Concrete and Rock,* Eds.: Shah S.P., Swartz S.E., SEM, Bethel, 192-207.